High Cationic Dispersity Boosted Oxygen Reduction Reactivity in Multi-Element Doped Perovskites

Li, Wenhuai; Li, Mengran; Guo, Yanan; Hu, Zhiwei; Zhou, Chuan; Brand, Helen E.A.; Peterson, Vanessa K.; Pao, Chih Wen; Chen, Chien Te; More Authors

Important note
To cite this publication, please use the final published version (if applicable).
Please check the document version above.

RESEARCH ARTICLE

High Cationic Dispersity Boosted Oxygen Reduction Reactivity in Multi-Element Doped Perovskites

Wenhuai Li, Mengran Li, Yanan Guo, Zhiwei Hu, Chuan Zhou, Helen E. A. Brand, Vanessa K. Peterson, Chih-Wen Pao, Hong-Ji Lin, Chien-Te Chen, Wei Zhou,* and Zongping Shao

Oxygen-ion conducting perovskite oxides are important functional materials for solid oxide fuel cells and oxygen-permeable membranes operating at high temperatures (>500 °C). Co-doped perovskites have recently shown their potential to boost oxygen-related kinetics, but challenges remain in understanding the underlying mechanisms. This study unveils the local cation arrangement as a new key factor controlling oxygen kinetics in perovskite oxides. By single- and co-doping Nb^{5+} and Ta^{5+} into $SrCoO_{3-\delta}$, dominant factors affecting oxygen kinetics, such as lattice geometry, cobalt states, and oxygen vacancies, which are confirmed by neutron and synchrotron X-ray diffraction as well as high-temperature X-ray absorption spectroscopy, are controlled. The combined experimental and theoretical study unveils that co-doping likely leads to higher cation dispersion at the B-site compared to single-doping. Consequently, a high-entropy configuration enhances oxygen ion migration in the lattice, translating to improved oxygen reduction activity.

1. Introduction

The oxygen reduction reaction (ORR) that reduces molecular oxygen to oxygen ions underpins many energy conversion and storage devices such as fuel cells and batteries.[1–4] Unlike most catalysis occurring at near-room temperature at surfaces, the ORR at temperatures above 500 °C involves both oxygen exchange at the catalyst surface and bulk diffusion within the catalyst lattice.[5,6] Efficient high-temperature ORR catalysts should possess both fast oxygen surface exchange kinetics and high bulk oxygen-ion conductivity. Most ORR catalysts are based on perovskite oxides with general formula ABO_3, where the A site contains 12-coordinated larger cations (e.g., alkaline earth, alkali, and lanthanoid elements) and the B site contains 6-coordinated smaller cations (e.g., transition metals such as Co, Fe, and Ni).[7–9] Oxygen-ion lattice conduction occurs through either oxygen vacancies or interstitial oxygen-ions, with the former mechanism most common among perovskite oxides.[10,11] Energetically favorable oxygen vacancy formation and fast oxygen migration are essential for a fast surface exchange.[12,13]

Substantial research has demonstrated the importance of lattice geometry, cation size, oxidation states, and electronegativity to ORR activity, with oxygen vacancy formation and mobility playing particularly important roles.[14–16] State-of-the-art ORR-active catalysts such as $Ba_{0.5}Sr_{0.5}Co_{0.8}Fe_{0.2}O_{3-\delta}$,[1,17] $SrCo_{0.8}Nb_{0.1}Ta_{0.1}O_{3-\delta}$ (SCNT),[12,18] and $PrBa_{0.5}Sr_{0.5}Co_{1.5}Fe_{0.5}O_{5+\delta}$[19] are perovskite oxide materials containing i) larger A-site cations with low charge (e.g., Sr^{2+} and Ba^{2+}), and ii) redox-active B-site cations (e.g., Co and Fe) partially doped with highly charged cations with relatively low electronegativity (e.g., Ta^{5+} as compared to Nb^{5+}). However, challenges remain to fully explain the synergistic effect of co-doping to enhance oxygen transport kinetics in perovskite materials. For example, our previous work showed that co-doping Nb^{5+} and Ta^{5+} with similar ionic size (0.64 Å) and slightly differing electronegativity (1.80 for Ta^{5+} and 1.87 for Nb^{5+}) at the B-site enables $SrCoO_{3-\delta}$[12,20,21] and $SrFeO_{3-\delta}$[22] with improved oxygen kinetics compared to their single-doped analogues. Similarly, co-doping at the B-site (e.g., Sc^{3+}/Nb^{5+} and Zr^{4+}/Y^{3+})[7,23] has also been reported to enhance oxygen kinetics and the ORR activity of perovskite oxides.

W. Li, Y. Guo, C. Zhou, W. Zhou, Z. Shao
State Key Laboratory of Materials-Oriented Chemical Engineering
College of Chemical Engineering
Nanjing Tech University
Nanjing 210009, P. R. China
E-mail: zhouwei1982@njtech.edu.cn

M. Li
Materials for Energy Conversion and Storage (MECS)
Department of Chemical Engineering
Faculty of Applied Sciences
Delft University of Technology
van der Maasweg 9, Delft 2629 HZ, The Netherlands

Z. Hu
Max-Planck-Institute for Chemical Physics of Solids
Nöthnitzer Str. 40 01187, Dresden, Germany

H. E. A. Brand
Australian Synchrotron
Australian Nuclear Science and Technology Organisation (ANSTO)
Clayton, Victoria 3168, Australia

V. K. Peterson
Australian Centre for Neutron Scattering
Australian Nuclear Science and Technology Organisation
Sydney, New South Wales, Australia

C.-W. Pao, H.-J. Lin, C.-T. Chen
National Synchrotron Radiation Research Center
101 Hsin-Ann Road, Hsinchu 30076, Taiwan

Considering that co-doped materials contain more than two types of cations at the B-site, we postulate that cation arrangement plays a particularly important role in controlling the ORR. This hypothesis comes from two general phenomena: first, the arrangement of the B-site host can be disrupted by co-substitution with an increasing number of dopants raising the configuration entropy of the B-site sub-lattice.[24,25] Second, the B-site cation arrangement has a profound impact on the oxygen-ion transport. Uberuaga and Pilania's theoretical study on the $SrLaTiAlO_6$ model double perovskite highlighted that the oxygen transport, including vacancy formation and mobility, is highly sensitive to the arrangement of B-site cations in the lattice: Ti/Al columnar ordering slowed oxygen-ion migration in the lattice due to its well-connected Ti configuration that poorly interacts with oxygen vacancies.[26] In contrast, previous studies of pyrochlore oxides showed that a disordered cation arrangement could both liberate oxygen vacancies within the structure and enhance oxygen migration.[27] Therefore, the cation arrangement (cation network) may contribute to the co-doping benefits to the ORR in perovskite oxides such as SCNT.

It remains challenging to understand the role of cation arrangement on oxygen kinetics experimentally, because co-doping in complex metal oxides normally changes structural geometry (e.g., lattice symmetry and free lattice volume), chemistry, and cation arrangement simultaneously. Herein, we study the effect of co-doping on the dispersity of B-site cations by examining the properties of $SrCo_{0.8}Nb_{0.2}O_{3-\delta}$ (SCN), $SrCo_{0.8}Ta_{0.2}O_{3-\delta}$ (SCT), and $SrCo_{0.8}Nb_{0.1}Ta_{0.1}O_{3-\delta}$ (SCNT) oxides that have very similar lattice geometry factors due to Nb^{5+} and Ta^{5+} dopants that have the same ionic radius and similar electronegativity.[12,21] Our experimental results unveil that co-doped SCNT has a slightly higher oxygen vacancy content and much-improved ORR activity as compared to the single-doped SCN and SCT materials. This is likely a result of an increased level of B-site cation dispersion originating from a high configuration entropy. Consequently, such highly-dispersed cation arrangements significantly improve ORR activity by liberating oxygen vacancies and enhancing the overall oxygen-ion mobility.

2. Results and Discussion

2.1. Structural Characterization

Neutron, synchrotron and laboratory X-ray powder diffraction at room temperature all show that the synthesized SCN, SCNT, and SCT samples quenched from 600 °C are cubic perovskite structures with space group symmetry $Pm\overline{3}m$ (see **Figure 1**; Figure S1, Supporting Information). Joint Rietveld refinement using these data (Table S1, Supporting Information) reveals lattice constants of 3.90357(3) Å for SCN, 3.90820(4) Å for SCT, and 3.90402(3) Å for SCNT. All three samples show similar crystal structure and lattice constants, which arise from the similar ionic size of Nb^{5+} and Ta^{5+}. High-resolution transmission electron microscopy (HRTEM) further confirmed the structures of the three samples. As shown in Figure S2 (Supporting Information), the lattice fringe distance is 0.275 nm for SCN, 0.275 nm for SNCT, and 0.274 nm for SCT, consistent with the (110) lattice spacing. We therefore confirm

that the SCN, SCNT, and SCT materials have similar lattice geometry (see Note S1, Supporting Information), enabling the role of the B-site cation arrangement on oxygen kinetics to be explored in this system.

2.2. Comparison of Cobalt States and Oxygen Vacancies

All elements in SCN, SCNT, and SCT except cobalt (i.e., Sr^{2+}, Nb^{5+}, and Ta^{5+}) should be stable at elevated temperatures. As the ORR-active metal centers, cobalt ions are essential to creating oxygen vacancies that facilitate oxygen mobility.[28–30] Therefore, we studied the valence states of cobalt in bulk SCN, SCNT, and SCT samples made into electrodes of a symmetrical cell by employing hard X-ray absorption spectroscopy (XAS) at room temperature, 500 °C, and 600 °C. The symmetric cell is supported by a $Gd_{0.1}Ce_{0.9}O_{1.95}$ (GDC) electrolyte disk, where samples were deposited on both sides of the disk as the electrodes. Each of the prepared cells was characterized by XAS during heating in a high-temperature reaction chamber.

The Co-K edge X-ray absorption near-edge spectroscopy (XANES) are shown in **Figure 2**a–c. At room temperature in Figure 2a, the cobalt valence in SCNT is slightly lower than in SCT and SCN, as evidenced by the shift of the absorption edge toward lower energy.[31–33] At elevated temperatures, particularly at 600 °C in Figure 2c, the absorption edge in all three samples becomes similar and shifts to the lower energy relative to room temperature as shown in Figure S4a (Supporting Information), indicating that cobalt ions have similar and reduced valence states at operating temperatures. These results are further confirmed by thermogravimetry as shown in Figure S3 (Supporting Information). The results clearly show that oxygen vacancies are created when the cobalt valence state reduces. In order to further probe the Co valence and oxygen content, we compared XANES results with standards of different Co valence and calculated that the bulk average valence of Co in SCNT at 600 °C is 2.75, as shown in Figure S4 (Supporting Information). Considering a similar cobalt occupancy (i.e., 80% at the B-site) and valence states, we postulate a similar oxygen content (δ is 0.400 according to the principle of electric neutrality) of all three samples. Structural refinement using NPD data (Table S1, Supporting Information) confirm that SCNT has a slightly lower oxygen occupancy at 85.1(4)% than SCN at 85.5(6)% and SCT at 86.3(5)%. Accordingly, SCNT has a slightly higher oxygen non-stoichiometry (0.477 ± 0.012) to SCN (0.435 ± 0.018) and SCT (0.411 ± 0.015).

In addition to bulk oxygen diffusion, the oxygen surface exchange also determines the overall activity of the oxygen reduction at elevated temperatures by affecting surface oxygen adsorption, dissociation, and oxygen vacancy migration.[34–36] Hence, we also studied the electronic structure of cobalt ion at the surface using soft XAS. As compared to hard XAS, soft XAS in total electron yield mode at the Co-L_3 edge is sensitive to a $\approx$5 nm depth, allowing the study of the cobalt valence state at the surface. The further advantage of soft XAS is the highly sensitive to spin state[37–39] and local environment[40,41] of Co ions in the different valence states.

Figure 2d compares Co-L_3 edge XAS data for all three samples at room temperature. The left and right edges of the
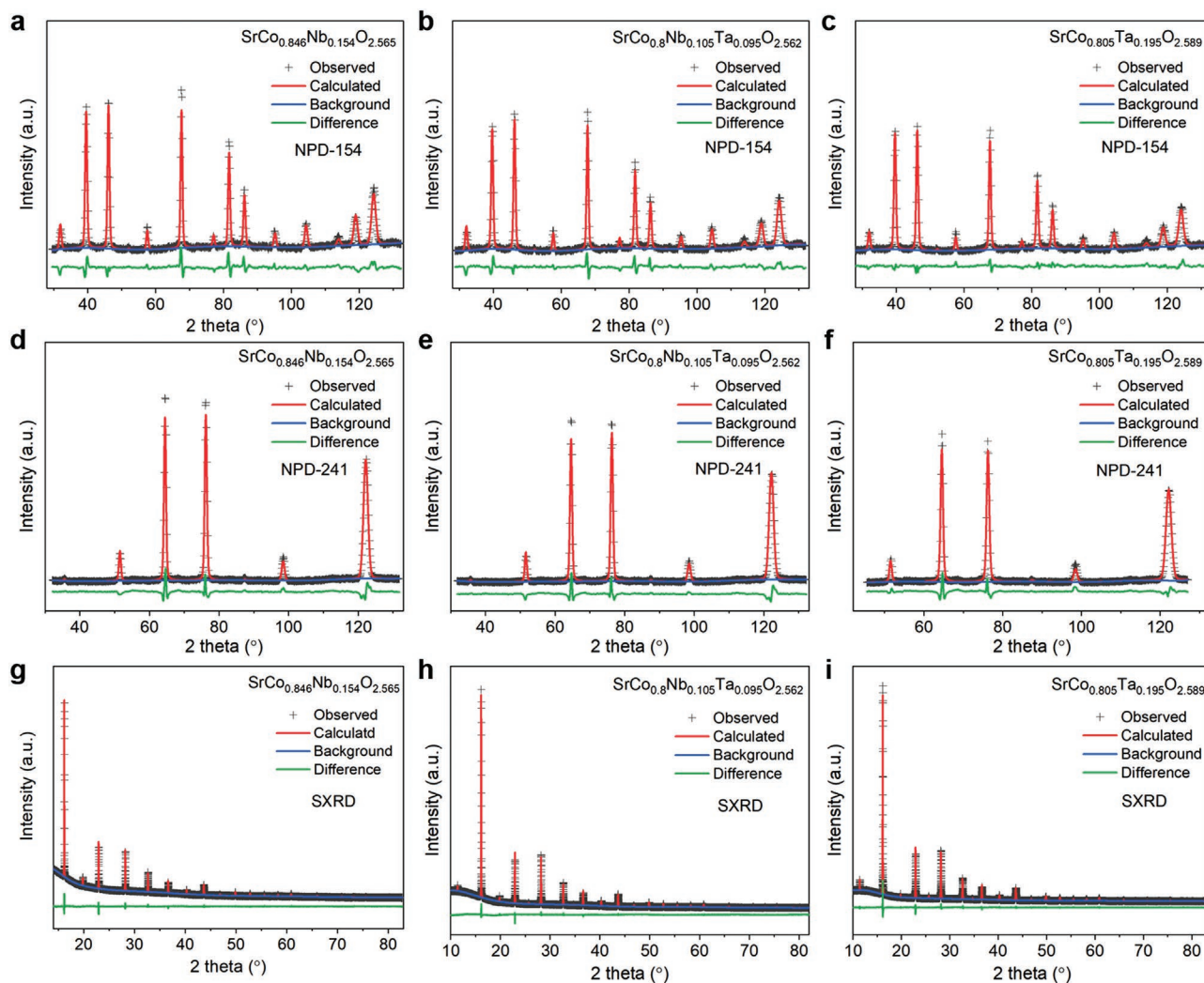
Figure 1. Joint Rietveld refinement profile of a,d,g) SCN, b,e,h) SCNT, and c,f,i) SCT powders quenched at 600 °C using both neutron and synchrotron X-ray powder diffraction data. NPD-154 and NPD-241 are neutron powder diffraction data at neutron wavelengths of approximately 1.54 and 1.64 Å, respectively. Refinement results are given in Table S1 (Supporting Information).

data contain contributions from different valence and spin states. All samples are similar in terms of energy position and shape, indicating that the cobalt valence and spin states are similar.[12,21] We simulated the experimental Co-L_3 XAS data of all samples to determine the Co valence and spin state and superposed this onto the relevant reference spectra CoO for Co^{2+}, $EuCoO_3$ for low-spin (LS) Co^{3+},[42] and Sr_2CoRuO_6 for high-spin (HS) Co^{3+}[43] (Figure 2e). This revealed that surface cobalt ions have an average valence of +2.95 and contain a mixture of cobalt states: ≈10% Co^{2+}, 75% HS Co^{3+}, and 15% LS Co^{3+} for all samples at the surface.

Further, we performed X-ray photoelectron spectroscopy (XPS) to investigate the surface Co valence of the three samples at room temperature (Figure 2f). The similar binding energies for Co 2p peaks in XPS data of SCN, SCNT, and SCT indicate a negligible difference in the state of Co at the surface in all samples. Additionally, we evaluated the similarity of cobalt spin states through the field dependence of the magnetization of SCN, SCNT, and SCT at room temperature. As shown
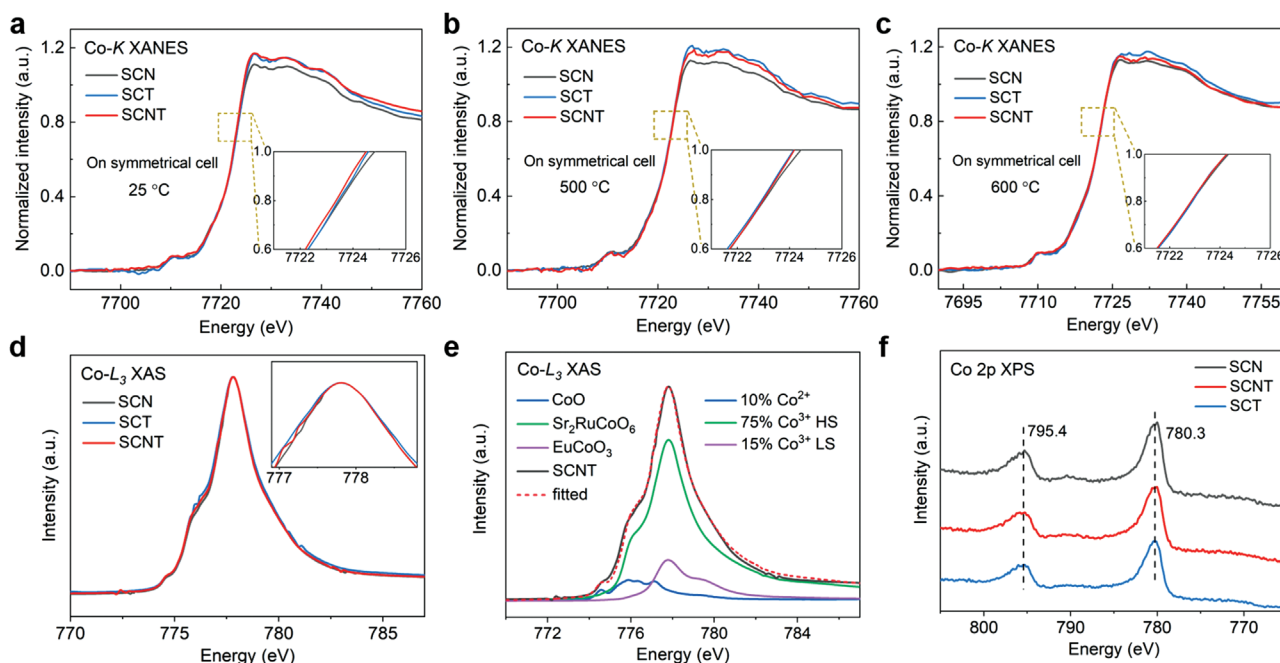
in Figure S5 (Supporting Information), data are straight lines with an insignificant hysteresis loop, indicating that the three samples all exhibit the same paramagnetism, i.e., similar cobalt outer electron spin states.

Taken together, our experimental results show that the SCN, SCNT, and SCT materials have similar states of cobalt at both the surface and in the bulk. If the arrangement of the B-site cations is highly disordered, we should expect similar ORR activity for all samples.

2.3. ORR Activity Comparison

Contradictory to our expectations, the ORR activity significantly differs among these three samples. Nyquist plots using electrochemical impedance spectroscopy (EIS) measurements of symmetric cells containing SCN, SCNT, or SCT are shown in Figure S6 (Supporting Information). The polarization resistance was determined by the difference of the intercepts of the

**ADVANCED
SCIENCE NEWS**
www.advancedsciencenews.com

**ADVANCED
FUNCTIONAL
MATERIALS**
www.afm-journal.de

Figure 2. Co K-edge XANES data of SCN, SCNT, and SCT at a) 25 °C, b) 500 °C, and c) 600 °C. d) Co-L_3 XAS data of SCN, SCNT, and SCT. e) SCNT Co-L_3 XAS data (black line) and quantitative calculations (red dashed line) of contributions determined from standards for Co^{2+} (blue line), HS Co^{3+} (green line), LS Co^{3+} (purple line). f) Co 2p XPS data of SCN, SCNT, and SCT. Vertical dotted lines at identified energies are guides to the eye.

area-specific resistance (ASR) with the real axis. A low ASR value indicates a high ORR activity. The SCNT achieved a low ASR of 0.12 Ω cm² at 500 °C, which is far better than SCN (0.29 Ω cm²) and SCT (0.21 Ω cm²) under the same conditions (**Figure 3**). Further, the activation energy of SCNT is much lower than for SCN or SCT. Therefore, SCNT outperforms SCN and SCT materials at reduced operating temperatures, a trend that is consistent with our previous work.[12] Such discernable

ORR activity improvement over SCNT is challenging to explain given the similar states of cobalt for the samples.

2.4. The Role of B-Site Cation Arrangement in Determining Perovskite Activity

Doping of Nb^{5+} and Ta^{5+} into $SrCoO_{3-\delta}$ created three different perovskite materials with similar lattice geometry, as well as bulk and surface cobalt states, allowing the effects of the *B*-site cation arrangement on the ORR to be studied. Although these three perovskite oxides are generally assumed to have a disordered *B*-site cation arrangement, co-doping Nb^{5+} and Ta^{5+} should lead to a higher configuration entropy (S_{conf}), with high dispersion of *B*-site cations with reduced aggregation. The S_{conf} of $SrCo_{1-x-y}Nb_xTa_yO_{3-\delta}$ series perovskite oxides can be calculated by Equation (1).[44]

$$S_{conf} = -R\left\{(1-x-y)\ln(1-x-y) + x\ln x + y\ln y\right\} \qquad (1)$$

where *R* is molar gas constant, and the same Sr and oxygen vacancy content are assumed, noting that oxygen vacancies for these materials range from 13.7(5)% for SCT to 14.9(6)% for SCNT. S_{conf}, in J mol⁻¹ K⁻¹, is calculated as 4.1603 for SCT, 4.1603 for SCN, and 5.3129 for SCNT.

We postulate that the *B*-site cation arrangement will have a significant impact on oxygen mobility by affecting the migration of oxygen vacancies at the surface and influencing the oxygen diffusion path. A highly dispersed arrangement of cations facilitates the fast migration of oxygen vacancies (see the illustration in **Figure 4**), with the high configuration entropy of SCNT likely enabling oxygen migration at both surface and
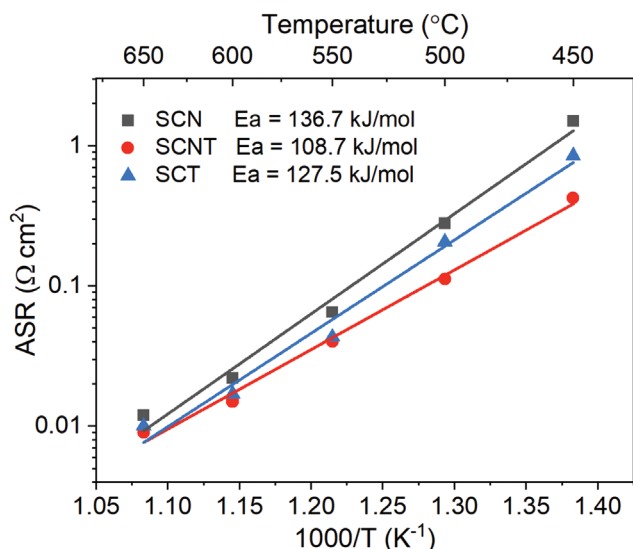
Figure 3. Thermal evolution of the ASR of SCN, SCNT, and SCT cathodes as prepared and studied under the same conditions, determined using electrochemical impedance spectroscopy (EIS) in a $Gd_{0.1}Ce_{0.9}O_{1.95}$ (GDC)-based symmetrical cell.
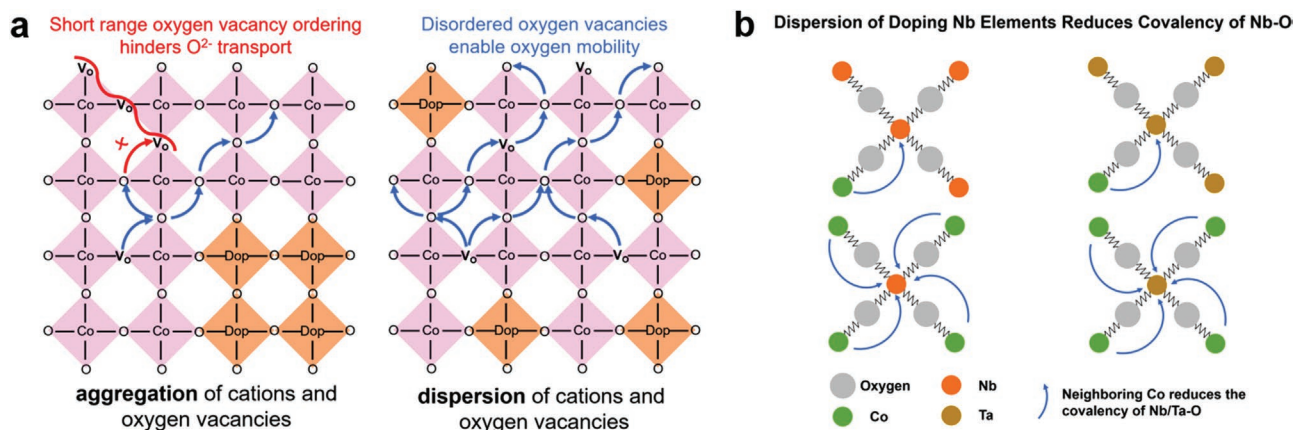
Figure 4. a) Schematic of oxygen vacancy distribution in perovskite lattice with different degree of aggregation of cations (The "Dop" in schematic represents the dopants in perovskite lattice). b) Different surroundings of dopants influence dopant-oxygen covalency.

bulk, thereby improving ORR activity.[7,45–47] As it is challenging to directly probe the cation arrangement, we explore the link between dopant-oxygen covalency and cation arrangement using density functional theory (DFT) calculations.

Cation arrangement impacts lattice dopant-oxygen chemistry, and we consider the number of nearest neighbor cobalt ions to the dopant as an attribute of the cation arrangement. A dopant surrounded by more cobalt has reduced dopant-oxygen covalency due to the delocalization of cobalt ion electrons (Figure 4b). Therefore, a highly connected network of cobalt can be used to understand the impact of cation arrangement on ORR activity through dopant-oxygen covalency. Electron localization function (ELF) maps visualize electron density and aid in characterizing metal-oxygen covalency in our Nb- and Ta-doped structural models (**Figure 5**; Figure S10, Supporting Information), with high ELF values along a bond indicating strong covalency (discussed in Note S2, Supporting Information), see Experimental Section for model details.[48–50] Importantly, as shown in Figure S12 (Supporting Information), ELF values along dopant-oxygen bonds increase significantly as dopants aggregate, with ELF values increasing in order: ELF_{SCN1} (0.245) < ELF_{SCN2} (0.253) < ELF_{SCN3} (0.255) < ELF_{SCN4} (0.262); ELF_{SCT1} (0.302) < ELF_{SCT2} (0.316) < ELF_{SCT3} (0.318) < ELF_{SCT4} (0.323).

We also calculated the configuration entropy for structural models with different cation dispersion. Using the Nb-doped sample as an example, we calculate the configuration entropy (S_{conf} in J mol^{-1} K^{-1}) of structures of formulae $SrCo_{0.8}(Nb_1)_{0.2}O_{3-\delta}$ = SCN1 of 4.1603 > $SrCo_{0.8}(Nb_2)_{0.2/2}O_{3-\delta}$ = SCN2 of 3.3984 > $SrCo_{0.8}(Nb_3)_{0.2/3}O_{3-\delta}$ = SCN3 of 2.9852 > $SrCo_{0.8}(Nb_4)_{0.2/4}O_{3-\delta}$ = SCN4 of 2.7295. Similarly, for SCT we calculate configuration entropy in J mol^{-1} K^{-1} of 4.1603 for SCT1 > 3.3984 for SCT2 > 2.9852 for SCT3 > 2.7295 for SCT4 (see Figure 5d). These calculations show that aggregation of dopants (increased configuration entropy) lead to lower dopant-oxygen covalency. These results explain the significantly improved ORR activity for SCNT, and we find that in the SCN1T1 model (Figure 5c and Figure S11, Supporting Information), ELF values along dopant-oxygen bonds are 0.246 for Nb-O and 0.303 for Ta-O, comparable to SCN1 and SCT1 models, where cobalt ions are well connected at the B-site. Therefore,

we conclude that the B-site cation arrangement is central to determining oxygen ion migration and ORR activity.
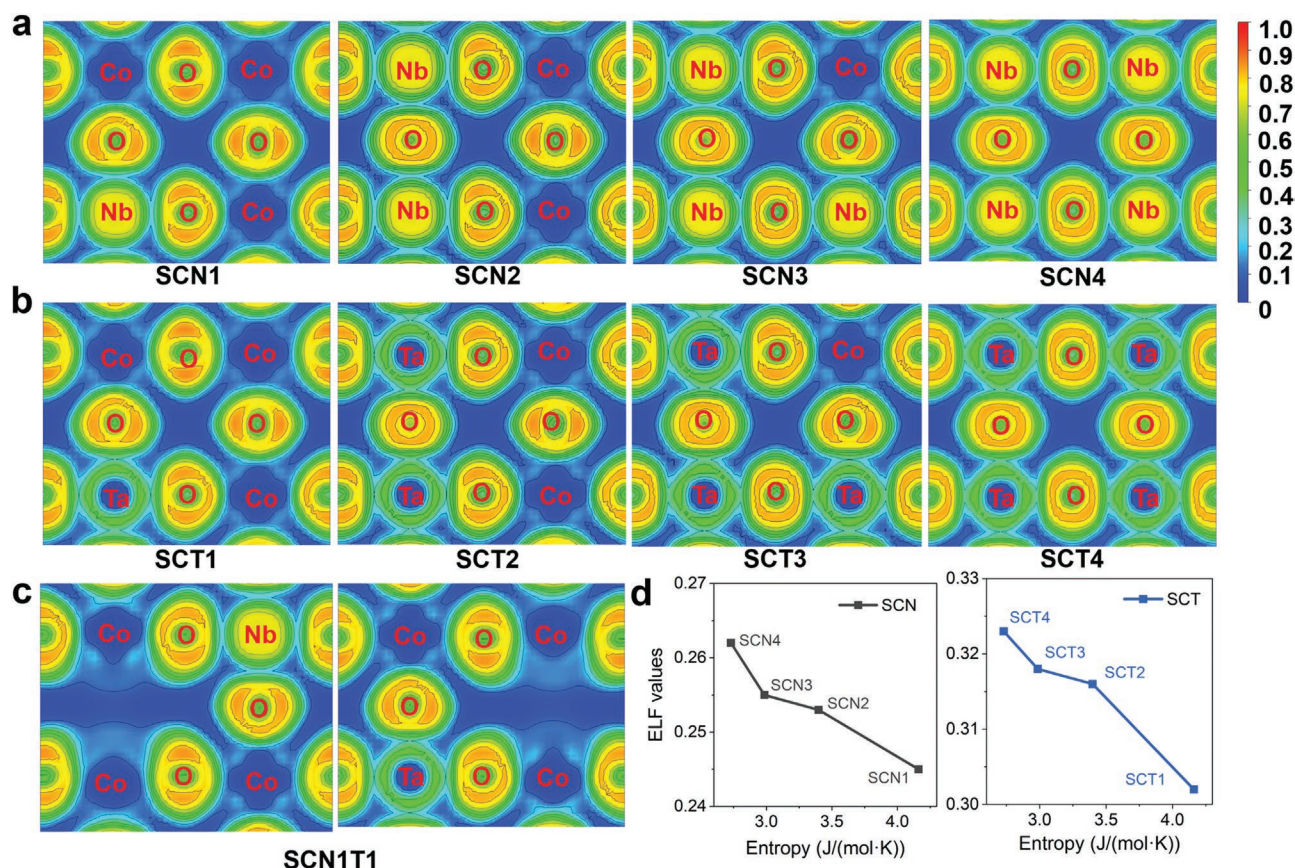
3. Conclusion

In summary, we present the underlying mechanism for enhanced ORR activity of co-doped $SrCo_{0.8}Nb_{0.105}Ta_{0.095}O_{2.562}$ compared to single-doped $SrCo_{0.846}Nb_{0.154}O_{2.565}$ and $SrCo_{0.805}Ta_{0.195}O_{2.589}$ materials. Single- or co-doping Nb^{5+} and Ta^{5+} with similar size and charge enabled the synthesis of three isostructural perovskite oxides with similar states of ORR-active cobalt ions. Combined Co-K edge X-ray absorption and computational results show that the co-doped Nb^{5+} and Ta^{5+} sample has a similar cobalt state but higher cation dispersion compared to single-doped counterparts. Our studies reveal that high dopant dispersion enhances oxygen vacancy migration and therefore ORR activity, achieved through increased configuration entropy. This work provides a new strategy for the development of advanced high oxygen ion conductors for solid oxide fuel cells and similar applications.

4. Experimental Section

Sample Synthesis: SCNT was synthesized via a solid-state reaction using $SrCO_3$, Co_3O_4, Nb_2O_5, and Ta_2O_5 (≥99%, Aladdin). Stoichiometric reagents were mixed in a planetary mill (Fritsch, Pulverisette 5) in ethanol at 400 rpm for 2 h. After drying, the primary powders were calcined at 1200 °C in air for 12 h, and the sintered pellets were well ground and re-sintered for another 10 h at 1200 °C to form perovskite oxide. SCN and SCT were also prepared similarly.

Structure Characterization: X-ray diffraction (XRD) data of SCN, SCNT, and SCT were obtained on a Rigaku Smartlab diffractometer using filtered Cu-Kα radiation (λ = 1.5418 Å). Synchrotron XRD data were collected at the Australian Synchrotron, Australian Nuclear Science and Technology Organization (ANSTO) with λ = 0.7746600(5) Å and a data collection time of 180 s per detector position. Neutron powder diffraction (NPD) data were collected using the high intensity neutron powder diffractometer Wombat at ANSTO (λ = 1.545016(462) Å and λ = 2.419487(513) Å). The wavelengths of the NPD and synchrotron XRD beams were determined using data for the NIST (National

**ADVANCED
SCIENCE NEWS**

www.advancedsciencenews.com

**ADVANCED
FUNCTIONAL
MATERIALS**

www.afm-journal.de

Figure 5. ELF maps for model (001) planes of a) SCN, b) SCT, and c) SCNT. The BO_6 octahedron contains six B-O bonds, the ELF values for which are obtained by combining the ELF values for the (100) and (001) planes. d) Variation of ELF values along dopant-oxygen bonds shown for various SCN and SCT models with differing configuration entropy. Models are shown in Figures S7–S9 (Supporting Information). Lines through the points are guides to the eye.

Institute of Standards and Technology) standard reference material LaB_6 660b. GSAS-II was employed to perform combined Rietveld analysis using the synchrotron XRD and NPD data using a starting phase with $Pm\bar{3}m$ space group symmetry.[12] High resolution transmission electron microscopy (HR-TEM) data were collected using a Tecnai G2 F20 S-TWIN microscope operating at 200 kV. X-ray photoelectron spectra (XPS) were obtained using a PHI5000 VersaProbe spectrometer with an Al-Kα X-ray source. The Co-K X-ray absorption near edge as a function of temperature and soft X-ray absorption spectroscopy at the Co-L_3 were performed at the Taiwan Photon Source BL44A as well as the Taiwan Light Source (TLS) BL07A and BL11A, respectively of the National Synchrotron Radiation Research Center in Taiwan. Temperature dependent data were collected after the sample was held at temperature for 30 min. The photon energies of the Co K-edge were calibrated using metal Co foils as references. CoO single crystals was measured simultaneously for the calibration of the energy scales of Co L_3 spectra.

Electrochemical Measurements: Symmetrical cells with the SCNT|GDC|SCNT configuration were fabricated for impedance studies. Dense $Gd_{0.1}Ce_{0.9}O_{1.95}$ (GDC) disks, 10.1 mm in diameter and 0.8 mm thick, were prepared through dry pressing. The disks were then sintered at 1350 °C for 5 h. SCNT cathode powder was first dispersed in a premixed solution of glycerol, ethylene glycol, and isopropyl alcohol, forming a colloidal suspension via planetary milling (Fritsch, Pulverisette 5) at 400 rpm for 0.5 h. The resulting slurry was sprayed onto both surfaces of the GDC pellet symmetrically and calcined at 900 °C for 2 h in air. Silver paste was used as the current collector. The thickness of the cathode was controlled by spraying time. EIS of the symmetrical cells were obtained in the air using a Solartron 1287 potentiostat and a

1260 A frequency response analyzer. The frequency range was 0.01 Hz to 100 kHz and the signal amplitude was 10 mV under open cell voltage conditions. The cathode polarization resistance of SCN and SCT were measured in the same way.

Density Functional Theory Calculations: Periodic density functional theory (DFT) calculations were performed using the plane wave basis in the Vienna Ab-initio Simulation Package (VASP).[51] The electron-exchange correlation function was treated using the Perdew–Burke–Ernzerhof (PBE) functional within the generalized gradient approximation (GGA).[52] Electron-core interactions were treated by the projector augmented wavefunction (PAW) method.[53] The PAW potentials explicitly included 10 valence electrons for Sr ($4s^24p^65s^2$), 9 for Co ($3d^84s^1$), 6 for O ($2s^22p^4$), 11 for Ta ($5p^65d^36s^2$), and 11 for Nb ($4p^64d^45s^1$). The gamma centered $5 \times 5 \times 5$ Monkhorst-Pack k-point grid in the Brillouin zone was applied for a $2 \times 2 \times 3$ supercell.[54] A width of 0.1 eV was employed for Gaussian smearing. The kinetic energy cut-off of the plane wave basis set was set to 600 eV with an energy precision of 1.0×10^{-6} eV. The atomic positions and lattice constants were fully optimized using the conjugate gradient (CG) scheme until the maximum force on each atom was smaller than 0.01 eV Å^{-1}. The localized d electrons of Co, Ta, and Nb were treated using the corrected exchange-correlation functional with a Hubbard-like term (GGA+U method).[55] The on-site coulomb interaction parameter (U-J) = 0.8 eV was employed for Co d electrons. This U-J value was qualified in previous calculations using the same GGA functional as the current study to produce lattice parameters and magnetic moments which are in good agreements with experimental measurements.[7] The same settings were applied to Ta and Nb in the doped systems.

**ADVANCED
SCIENCE NEWS**

www.advancedsciencenews.com

**ADVANCED
FUNCTIONAL
MATERIALS**

www.afm-journal.de

The SrCoO$_3$ crystal structure with space group of $Pm\overline{3}m$ was used as a starting model.[56,57] A geometrically optimized $2 \times 2 \times 3$ supercell of SrCoO$_3$ was used to carefully construct a series of single- and co-doped models. In order to study the relationship between the dispersity of doped Nb (Ta) and the corresponding Nb-O (Ta-O) covalency, four models were designed, i.e., one, two, three, and four neighboring Co ions were replaced by Nb (Ta) ions, which were named as SCN1 (SCT1), SCN2 (SCT2), SCN3 (SCT3), and SCN4 (SCT4), respectively (Figures S7 and S8, Supporting Information). The four models represent Nb (Ta) aggregation degrees from low to high. Two distant Co ions were replaced by Nb and Ta ions, respectively, in the co-doped model, named SCN1T1 (Figure S9, Supporting Information). Two distant oxygen vacancies were included in each model as informed by experimental observations from XANES.

Supporting Information

Supporting Information is available from the Wiley Online Library or from the author.

Conflict of Interest

The authors declare no conflict of interest.

Data Availability Statement

Research data are not shared.

[1] Z. Shao, S. M. Haile, *Nature* **2004**, *431*, 170.

[2] Y. G. Zhu, X. Wang, C. Jia, J. Yang, Q. Wang, *ACS Catal.* **2016**, *6*, 6191.

[3] X. Feng, Y. Bai, M. Liu, Y. Li, H. Yang, X. Wang, C. Wu, *Energy Environ. Sci.* **2021**, *14*, 2036.

[4] Y. Zhang, B. Chen, D. Guan, M. Xu, R. Ran, M. Ni, W. Zhou, R. O'Hayre, Z. Shao, *Nature* **2021**, *591*, 246.

[5] T. Ishigaki, S. Yamauchi, K. Kishio, J. Mizusaki, K. Fueki, *J. Solid State Chem.* **1988**, *73*, 179.

[6] Y. Song, Y. Chen, M. Xu, W. Wang, Y. Zhang, G. Yang, R. Ran, W. Zhou, Z. Shao, *Adv. Mater.* **2020**, *32*, 1906979.

[7] W. Zhou, J. Sunarso, M. Zhao, F. Liang, T. Klande, A. Feldhoff, *Angew. Chem., Int. Ed.* **2013**, *52*, 14036.

[8] D. Zhang, Y. Song, Z. Du, L. Wang, Y. Li, J. B. Goodenough, *J. Mater. Chem. A* **2015**, *3*, 9421.

[9] C. Yao, J. Yang, S. Chen, J. Meng, K. Cai, Q. Zhang, *J. Alloys Compd.* **2021**, *868*, 159127.

[10] M. Mogensen, D. Lybye, N. Bonanos, P. Hendriksen, F. Poulsen, *Solid State Ion* **2004**, *174*, 279.

[11] A. Chroneos, B. Yildiz, A. Tarancón, D. Parfitt, J. A. Kilner, *Energy Environ. Sci.* **2011**, *4*, 2774.

[12] M. Li, M. Zhao, F. Li, W. Zhou, V. K. Peterson, X. Xu, Z. Shao, I. Gentle, Z. Zhu, *Nat. Commun.* **2017**, *8*, 13990.

[13] C. L. Hanselman, D. N. Tafen, D. R. Alfonso, J. W. Lekse, C. Matranga, D. C. Miller, C. E. Gounaris, *Comput. Chem. Eng.* **2019**, *126*, 168.

[14] M. Li, W. Zhou, Z. Zhu, *Asia-Pac. J. Chem. Eng.* **2016**, *11*, 370.

[15] X. Mao, Z. Li, M. Li, X. Xu, C. Yan, Z. Zhu, A. Du, *J. Am. Chem. Soc.* **2021**, *143*, 9507.

[16] H. Gu, M. Xu, Y. Song, C. Zhou, C. Su, W. Wang, R. Ran, W. Zhou, Z. Shao, *Compos. B. Eng.* **2021**, *213*, 108726.

[17] W. Zhou, R. Ran, Z. Shao, W. Jin, N. Xu, *J. Power Sources* **2008**, *182*, 24.

[18] X. Ding, Z. Gao, D. Ding, X. Zhao, H. Hou, S. Zhang, G. Yuan, *Appl Catal B* **2019**, *243*, 546.

[19] J. Zan, S. Wang, D. Zheng, F. Li, W. Chen, Q. Pei, L. Jiang, *Mater. Res. Bul.* **2021**, *137*, 111173.

[20] W. Zhou, W. Jin, Z. Zhu, Z. Shao, *Int. J. Hydrog.* **2010**, *35*, 1356.

[21] M. Li, W. Zhou, V. K. Peterson, M. Zhao, Z. Zhu, *J. Mater. Chem. A* **2015**, *3*, 24064.

[22] Q. Zhou, L. Zhang, T. He, *Electrochem. Comm.* **2010**, *12*, 285.

[23] C. Duan, D. Hook, Y. Chen, J. Tong, R. O'Hayre, *Energy Environ. Sci.* **2017**, *10*, 176.

[24] L. Shen, Z. Du, Y. Zhang, X. Dong, H. Zhao, *Appl. Catal. B* **2021**, *295*, 120264.

[25] C. Oses, C. Toher, S. Curtarolo, *Nat. Rev. Mater.* **2020**, *5*, 295.

[26] B. P. Uberuaga, G. Pilania, *Chem. Mater.* **2015**, *27*, 5020.

[27] J. Shamblin, M. Feygenson, J. Neuefeind, C. L. Tracy, F. Zhang, S. Finkeldei, D. Bosbach, H. Zhou, R. C. Ewing, M. Lang, *Nature Mater* **2016**, *15*, 507.

[28] W. Zhou, Z. Shao, R. Ran, R. Cai, *Electrochem. Comm.* **2008**, *10*, 1647.

[29] M. Li, W. Zhou, Z. Zhu, *ChemElectroChem* **2015**, *2*, 1331.

[30] V. Cascos, M. T. Fernández-Díaz, J. A. Alonso, *Renewable Energy* **2019**, *133*, 205.

[31] S. Agrestini, K. Chen, C.-Y. Kuo, L. Zhao, H.-J. Lin, C.-T. Chen, A. Rogalev, P. Ohresser, T.-S. Chan, S.-C. Weng, G. Auffermann, A. Völzke, A. C. Komarek, K. Yamaura, M. W. Haverkort, Z. Hu, L. H. Tjeng, *Phys. Rev. B* **2019**, *100*, 014443.

[32] Z. Liu, Y. Sakai, J. Yang, W. Li, Y. Liu, X. Ye, S. Qin, J. Chen, S. Agrestini, K. Chen, S.-C. Liao, S.-C. Haw, F. Baudelet, H. Ishii, T. Nishikubo, H. Ishizaki, T. Yamamoto, Z. Pan, M. Fukuda, K. Ohashi, K. Matsuno, A. Machida, T. Watanuki, S. I. Kawaguchi, A. M. Arevalo-Lopez, C. Jin, Z. Hu, J. P. Attfield, M. Azuma, Y. Long, *J. Am. Chem. Soc.* **2020**, *142*, 5731.

[33] D. Guan, G. Ryu, Z. Hu, J. Zhou, C.-L. Dong, Y.-C. Huang, K. Zhang, Y. Zhong, A. C. Komarek, M. Zhu, X. Wu, C.-W. Pao, C.-K. Chang, H.-J. Lin, C.-T. Chen, W. Zhou, Z. Shao, *Nat. Commun.* **2020**, *11*, 3376.

[34] Y. A. Mastrikov, R. Merkle, E. Heifets, E. A. Kotomin, J. Maier, *J. Phys. Chem. C* **2010**, *114*, 3017.

[35] J. H. Joo, R. Merkle, J. Maier, *J. Power Sources* **2011**, *196*, 7495.

[36] Z. Li, M. Li, Z. Zhu, *Electrochem. Energ. Rev.* **2021**.

**ADVANCED
SCIENCE NEWS**

www.advancedsciencenews.com

**ADVANCED
FUNCTIONAL
MATERIALS**

www.afm-journal.de

[37] Z. Hu, H. Wu, T. C. Koethe, S. N. Barilo, S. V. Shiryaev, G. L. Bychkov, H. H. Hsieh, H.-J. Lin, C. T. Chen, N. B. Brookes, S. Agrestini, Y.-Y. Chin, M. Rotter, L. H. Tjeng, *New J Phys* **2012**, *14*, 123025.

[38] Y. Y. Chin, Z. Hu, H.-J. Lin, S. Agrestini, J. Weinen, C. Martin, S. Hébert, A. Maignan, A. Tanaka, J. C. Cezar, N. B. Brookes, Y.-F. Liao, K.-D. Tsuei, C. T. Chen, D. I. Khomskii, L. H. Tjeng, *Phys. Rev. B* **2019**, *100*, 014443.

[39] S. Agrestini, C.-Y. Kuo, D. Mikhailova, K. Chen, P. Ohresser, T. W. Pi, H. Guo, A. C. Komarek, A. Tanaka, Z. Hu, L. H. Tjeng, *Phys. Rev. B* **2017**, *95*, 245131.

[40] H. Ohta, K. Yoshimura, Z. Hu, Y. Y. Chin, H.-J. Lin, H. H. Hsieh, C. T. Chen, L. H. Tjeng, *Phys. Rev. Lett.* **2011**, *107*, 066404.

[41] T. Burnus, Z. Hu, M. W. Haverkort, J. C. Cezar, D. Flahaut, V. Hardy, A. Maignan, N. B. Brookes, A. Tanaka, H.-H. Hsieh, H.-J. Lin, C.-T. Chen, L. H. Tjeng, *Phys. Rev. B* **2006**, *74*, 245111.

[42] Z. Hu, H. Wu, M. W. Haverkort, H. H. Hsieh, A. Tanaka, C. T. Chen, L. H. Tjeng, *Phys. Rev. Lett.* **2004**, *92*, 207402.

[43] J.-M. Chen, Y.-Y. Chin, M. Valldor, Z. Hu, J.-M. Lee, S.-C. Haw, N. Hiraoka, H. Ishii, C.-W. Pao, K.-D. Tsuei, J.-F. Lee, H.-J. Lin, L.-Y. Jang, A. Tanaka, C.-T. Chen, L. H. Tjeng, *J. Am. Chem. Soc.* **2014**, *136*, 1514.

[44] T. R. S. Prasanna, A. Navrotsky, *J. Mater. Res.* **1994**, *9*, 3121.

[45] Y. Tomura, I. Oikawa, H. Takamura, *Phys. Rev. Mater.* **2019**, *3*, 125802.

[46] R. van Doorn, *Solid State Ion* **2000**, *128*, 65.

[47] G. Liu, X. Li, Y. Wang, W. Liang, B. Liu, H. Feng, H. Yang, J. Zhang, J. Sun, *Appl. Surf. Sci.* **2017**, *425*, 121.

[48] A. Savin, R. Nesper, S. Wengert, T. F. Fässler, *Angew Chem Int Ed Engl* **1997**, *36*, 1808.

[49] Y. Xia, Y. Zhang, Q. Su, K. Dong, *ChemSusChem* **2020**, cssc.202001447.

[50] K. Koumpouras, J. A. Larsson, *J. Phys.: Condens. Matter* **2020**, *32*, 315502.

[51] G. Kresse, J. Furthmüller, *Phys. Rev. B* **1996**, *54*, 11169.

[52] J. P. Perdew, K. Burke, M. Ernzerhof, *Phys. Rev. Lett.* **1996**, *77*, 3865.

[53] G. Kresse, D. Joubert, *Phys. Rev. B* **1999**, *59*, 1758.

[54] H. J. Monkhorst, J. D. Pack, *Phys. Rev. B* **1976**, *13*, 5188.

[55] S. L. Dudarev, G. A. Botton, S. Y. Savrasov, C. J. Humphreys, A. P. Sutton, *Phys. Rev. B* **1998**, *57*, 1505.

[56] http://www.crystallography.net/cod/.

[57] Y. Long, Y. Kaneko, S. Ishiwata, Y. Taguchi, Y. Tokura, *J. Phys.: Condens. Matter* **2011**, *23*, 245601.